

# Lattice Wigner equation

S. Solórzano,<sup>1,\*</sup> M. Mendoza,<sup>1</sup> S. Succi,<sup>2</sup> and H. J. Herrmann<sup>1</sup>

<sup>1</sup>*ETH Zürich, Computational Physics for Engineering Materials,  
Institute for Building Materials, Wolfgang-Pauli-Str. 27, HIT, CH-8093 Zürich (Switzerland)*

<sup>2</sup>*Istituto per le Applicazioni del Calcolo C.N.R., Via dei Taurini, 19 00185 Rome,  
Italy and Institute for Advanced Computational Science, Harvard University*

We present a numerical scheme to solve the Wigner equation, based on a lattice discretization of momentum space. The moments of the Wigner function are recovered exactly, up to the desired order given by the number of discrete momenta retained in the discretisation, which also determines the accuracy of the method. The Wigner equation is equipped with an additional collision operator, designed in such a way as to ensure numerical stability without affecting the evolution of the relevant moments of the Wigner function. The lattice Wigner scheme is validated for the case of quantum harmonic and anharmonic potentials, showing good agreement with theoretical results. It is further applied to the study of the transport properties of one and two dimensional open quantum systems with potential barriers. Finally, the computational viability of the scheme for the case of three-dimensional open systems is also illustrated.

## I. INTRODUCTION

The phase-space formulation of quantum mechanics introduced by E.P. Wigner [1] back in 1932, has known a major surge of interest in the recent years, due to a mounting range of applications, from quantum chaotic systems [2, 3] and quantum optics [4] to ultracold atoms [5], for which the Wigner function has been experimentally reconstructed and measured via tomographic techniques.

From a theoretical perspective, the Wigner formulation is particularly appealing, because, by treating position and momentum as two independent quantities, it provides a close bridge between quantum mechanics and classical kinetic theory. [A bridge which turns into a complete reconnection in the limit of a vanishing de Broglie length](#) (See [6] and references therein). From a computational viewpoint, however, the Wigner equation is generally demanding and difficult to handle, its application being often limited to one-dimensional problems.

Different solution approaches have been proposed in the literature, such as collocation schemes [7–9], semi-classical methods [10, 11], Montecarlo approaches [12–15], finite differences [16–18], particle methods [19–21], and recently an approach in two dimensions has been proposed [22]. However, the numerical solution of the Wigner equation still stands as a difficult task, especially in three spatial dimensions.

Formally, the Wigner equation is similar to the Boltzmann equation, which permits us to borrow methods developed in computational kinetic theory to solve quantum mechanical problems. Of particular interest in this respect, is the Lattice Boltzmann (LB) method, a descendant of the lattice gas cellular gas automata [23, 24] which was originally introduced as an alternative to the discretisation of the Navier-Stokes equations of continuum

fluid mechanics [25–27].

Over the years, LB has been adapted to fields as diverse as quantum mechanics [28, 29], relativistic hydrodynamics [30], classical electrodynamics [31], and general relativity [32]. For a recent review, see [33]. The approach is in general computationally efficient and flexible, due to the local character of the lattice Boltzmann equation and the fact that information always propagates along straight characteristics (light-cones).

In this work, we formulate a lattice Wigner model, borrowing ideas and techniques from lattice Boltzmann schemes, namely, the use of a quadrature to reduce the momentum space to a small set of representative vectors, thus leading to substantial computational savings.

Even though our work is focussed on the collisionless Wigner equation, the present Lattice Wigner scheme includes a collision term, for the purpose of numerical stability [34].

Note that the collision operator is implemented in such a way as to preserve the dynamics of the Wigner function, i.e. the moments correctly reproduced by the numerical quadrature do not experience any dissipation.

For systems exhibiting genuinely physical dissipation, such constraint can be readily removed, so that only the conserved moments are conserved, while the non-conserved ones are indeed affected by dissipative effects.

The approach is validated for the case of both harmonic and anharmonic quantum oscillators and then applied to the transport properties of one and two-dimensional driven open quantum systems. Finally, we also show the capability of the model to handle 3D systems with soft potentials.

This paper is organized as follows: in section II, an introduction to the Wigner formalism is given, in section III the lattice Wigner model is derived in detail. In section IV, the model is validated and in section V it is applied to driven open quantum systems. Finally in section VI the main findings and conclusions are summarized.

---

\* [sosergio@ethz.ch](mailto:sosergio@ethz.ch)

## II. WIGNER FORMULATION

In this section, we provide the basic details about the Wigner formulation, for a comprehensive account see Ref. [35]. The Wigner formalism is a kinetic formulation of quantum mechanics physically equivalent to the Schrödinger representation [36]. The Wigner formulation, however, is very different, as it treats both position and momenta as independent variables, like in classical Hamiltonian dynamics and kinetic theory.

The Wigner function is defined as

$$\begin{aligned} W(\mathbf{q}, \mathbf{p}, t) &= \frac{1}{(2\pi\hbar)^d} \mathcal{W}(\hat{\rho}) \\ &= \frac{1}{(2\pi\hbar)^d} \int_{-\infty}^{\infty} d\mathbf{y} \rho(\mathbf{q} - \mathbf{y}/2, \mathbf{q} + \mathbf{y}/2) e^{i\mathbf{p} \cdot \mathbf{y}/\hbar}, \end{aligned} \quad (1)$$

where  $\rho(\mathbf{x}, \mathbf{x}')$  is the real space representation of the density matrix of the quantum system under consideration,  $d$  is the dimensionality of the system and the Weyl transform,  $\mathcal{W}(\cdot)$ , of a quantum mechanical operator  $\hat{O}$  is defined as:

$$\tilde{O}(\mathbf{q}, \mathbf{p}) = \mathcal{W}(\hat{O}) = \int e^{i\mathbf{p} \cdot \mathbf{y}/\hbar} \langle \mathbf{q} - \mathbf{y}/2 | \hat{O} | \mathbf{q} + \mathbf{y}/2 \rangle d\mathbf{y}. \quad (2)$$

In general,  $W(\mathbf{q}, \mathbf{p})$  is real and normalised in phase-space, i.e.  $\int d\mathbf{p} d\mathbf{q} W(\mathbf{p}, \mathbf{q}, t) = 1$ . However, due to quantum interference effects, it is not positive semidefinite, and consequently, it cannot be regarded as a proper distribution function, but rather as a *quasi*-distribution.

Expectation values of a physical observable  $\hat{O}$  are obtained through the prescription:

$$\text{tr}(\hat{\rho}\hat{O}) = \int d\mathbf{p} d\mathbf{q} \tilde{O}(\mathbf{q}, \mathbf{p}) W(\mathbf{p}, \mathbf{q}, t). \quad (3)$$

The moments of the Wigner function with respect to the momentum variable are defined as

$$\Pi(W)_{\alpha_1, \dots, \alpha_n}^n = \int d\mathbf{p} p_{\alpha_1} \dots p_{\alpha_n} W(\mathbf{q}, \mathbf{p}), \quad (4)$$

where  $n$  indicates the order of the moment and  $p_{\alpha_i}$  denotes the  $\alpha_i$  component of the momentum variable. The first two moments  $\Pi(W)^0$  and  $\Pi(W)_{\alpha_i}^1$  can be identified with the particle density  $\rho(\mathbf{x}, \mathbf{x})$  and momentum density respectively, whereas the sum of the diagonal terms of  $\Pi(W)_{\alpha_i \alpha_j}^2$  is proportional to the kinetic energy density.

The time evolution of the Wigner function can be obtained as the Weyl transform of the Liouville-von Neumann equation, namely:

$$\frac{\partial \hat{\rho}}{\partial t} = \frac{1}{i\hbar} [\hat{H}, \hat{\rho}],$$

where  $\hat{H} = \frac{\hat{\mathbf{p}}^2}{2m} + \hat{V}(\mathbf{x})$  is the Hamiltonian of the system.

The result is known as the Wigner equation and it reads as follows:

$$\frac{\partial W}{\partial t} + \frac{\mathbf{p}}{m} \cdot \nabla W + \Theta[V]W = 0, \quad (5)$$

where  $\Theta[V]W$  can be written as

$$\Theta[V]W = \int_{-\infty}^{\infty} \delta[V](\mathbf{q}, \mathbf{p} - \mathbf{p}') W(\mathbf{q}, \mathbf{p}') d\mathbf{p}' \quad (6)$$

$$\begin{aligned} \delta[V](q, p) &= \\ \frac{i}{2\pi\hbar^2} \int_{-\infty}^{\infty} (V(\mathbf{q} - \mathbf{y}/2) - V(\mathbf{q} + \mathbf{y}/2)) e^{i\mathbf{y} \cdot \mathbf{p}/\hbar} d\mathbf{y} \end{aligned} \quad (7)$$

or alternatively

$$\Theta[V]W = - \sum_{|\mathbf{s}| \in \mathbb{N}_{\text{odd}}} \left( \frac{\hbar}{2i} \right)^{|\mathbf{s}|-1} \frac{1}{s!} \frac{\partial^s V}{\partial q^s} \frac{\partial^s W}{\partial p^s}, \quad (8)$$

where  $\mathbf{s}$  is a vector of non negative integers,  $|\mathbf{s}| = \sum_{i=1}^d s_i$ ,  $\frac{\partial^s}{\partial a^s} \equiv \prod_{i=1}^d \frac{\partial^{s_i}}{\partial a^{s_i}}$  for  $a = \{q, p\}$ . Finally, it is important to notice that the different terms of the Wigner equation Eq.(5) can be linked to the different terms of the Liouville-von Neumann equation.

The convective term arises solely from the kinetic energy term in the Hamiltonian, whereas the force term  $\Theta[V]W$  originates from the potential energy contribution. To be noted that spatial derivatives of the potential at various orders couple to corresponding derivatives in momentum space, multiplied by the corresponding power of the Planck's constant  $\hbar$ . Such higher-order terms are responsible for the “quantumness” of the Wigner representation and the occurrence of negative values due to quantum interference effects.

## III. LATTICE WIGNER SCHEME

In this section, we introduce the lattice Wigner scheme in two subsequent stages. First, the space, time, and velocity discretisation of Eq.(5) is described, and subsequently, the details on the quadrature in momentum space are presented.

It is convenient to work in the dimensionless form of Eq.(5). Upon the change of variables  $q \rightarrow l_0 x$ ,  $p \rightarrow m(l_0/t_0)v$ ,  $t \rightarrow t_0\tau$  where  $x, v, \tau$  are the new dimensionless variables and  $l_0, t_0$  are characteristic length and time scales, respectively, Eq.(5) and Eq.(8) can be written as:

$$\frac{\partial \bar{W}}{\partial \tau} + \mathbf{v} \cdot \nabla_x \bar{W} + \Theta[V]\bar{W} = 0, \quad (9)$$

and

$$\Theta[V]\bar{W} = - \sum_{|\mathbf{s}| \in \mathbb{N}_{\text{odd}}} \left( \frac{H}{2i} \right)^{|\mathbf{s}|-1} \frac{1}{s!} \frac{\partial^s \bar{V}}{\partial x^s} \frac{\partial^s \bar{W}}{\partial v^s}, \quad (10)$$

where  $H = \frac{\hbar t_0}{m l_0^2}$ ,  $\bar{V} = \frac{V}{m(l_0/t_0)^2}$  are the dimensionless reduced Planck constant and potential terms, respectively. For convenience the relation between physical and dimensionless variables is given in Table. I

Variable	Physical	Lattice
Position	$q$	$x$
Momentum	$p$	$v$
Time	$t$	$\tau$
Reduced Planck constant	$\hbar$	$H$
Potential	$V$	$\bar{V}$
Wigner function	$W$	$\bar{W}$

TABLE I. Relation between physical and lattice variable symbols.

The space and time variables of Eq.(9) are discretized simultaneously, that is, first Eq.(9) is formally written as an ordinary differential equation along a  $\mathbf{x} + \mathbf{v}\delta\tau\lambda$  line (light-cone), with parameter  $\lambda \in [0, 1]$  and time step  $\delta\tau$

$$\frac{d\bar{W}}{d\lambda} = -\delta\tau\Theta[V]\bar{W},$$

This is then integrated leading to:

$$\bar{W}(\mathbf{x} + \mathbf{v}\delta t, \mathbf{v}, t + \delta t) - \bar{W}(\mathbf{x}, \mathbf{v}, t) = -\delta t\Theta[V]\bar{W}. \quad (11)$$

To be noted that that a first order Taylor series expansion of the l.h.s of Eq.(11) is consistent with Eq.(9).

The velocity space is discretized using quadratures instead of a regular grid approach. Besides avoiding the need of a finite cutoff in velocity space, which results in an inaccurate computation of the moments of the Wigner distribution, the quadrature approach also provides a better discretization of the  $\nabla$  operator[37].

In the present context, discretization by quadrature requires that the moments (Eq.(4)) in the velocity(momentum) space of  $\bar{W}$  and  $\Theta[V]\bar{W}$  can be calculated exactly. This is achieved using a set of  $N_q$  quadrature vectors and corresponding weights  $\{\mathbf{v}_i, w_i\}_{i=1}^{N_q}$ , obeying the consistency relations:

$$\begin{aligned} \Pi(\bar{W})_{\alpha_1, \alpha_1, \dots, \alpha_n}^n &= \int d\mathbf{v} v_{\alpha_1} v_{\alpha_1} \cdots v_{\alpha_n} \bar{W}(\mathbf{x}, \mathbf{v}, t) \quad (12) \\ &= \sum_{i=0}^{N_q} v_{i\alpha_1} v_{i\alpha_1} \cdots v_{i\alpha_n} w_i \bar{W}(\mathbf{x}, \mathbf{v}_i, t) \\ &= \sum_{i=0}^{N_q} v_{i\alpha_1} v_{i\alpha_1} \cdots v_{i\alpha_n} \bar{W}_i(\mathbf{x}, t), \end{aligned}$$

where  $\bar{W}_i(\mathbf{x}, t) = w_i \bar{W}(\mathbf{x}, \mathbf{v}_i, t)$  and  $v_{i\alpha_n}$  denotes the  $\alpha_n$  component of the  $i$ -th velocity vector. A similar set of equations holds for  $\Theta[V]\bar{W}$ .

Given a quadrature, Eq.(11) is further discretized as

$$\bar{W}_i(\mathbf{x} + \mathbf{v}_i\delta t, t + \delta t) - \bar{W}_i(\mathbf{x}, t) = -\delta t(\Theta[V]\bar{W})_i. \quad (13)$$

Following the lattice Boltzmann nomenclature, the  $\bar{W}_i$  and  $(\Theta[V]\bar{W})_i$  are termed respectively “distributions” and “source distributions”. Observe that the time evolution of the distributions is given by Eq.(13) and that at every spatial lattice point  $\mathbf{x}$ , there are  $N_q$  distributions,

from which the moments, such as density  $\Pi(\bar{W})^0 = \rho$  or momentum density  $\Pi(\bar{W})_{\alpha}^1 = \rho u_{\alpha}$ , can be calculated at every time step using Eq.(12).

It is important to notice that, although a discretization by quadrature requires no cutoff in velocity space, it does nonetheless involve a ceiling on the highest moment for which Eq.(12) holds. In other words, it is a truncation in discrete momentum space.

It is in principle possible to use Eq.(13) to track the time evolution of the moments of the Wigner function under the action of a specified potential. However, it was shown in Ref. [34] that the resulting structure of the forcing term leads to numerical instabilities. To address this problem, the lattice Wigner model is introduced as

$$\begin{aligned} \bar{W}_i(\mathbf{x} + \mathbf{v}_i\delta t, t + \delta t) - \bar{W}_i(\mathbf{x}, t) &= \delta t\Omega_i + \delta tS_i + \\ \frac{\delta t}{2} (S_i(\mathbf{x}, t) - S_i(\mathbf{x} - \mathbf{v}_i\delta t, t - \delta t)) & \quad (14) \\ \Omega_i &= -\frac{1}{\tau_w}(\bar{W}_i(\mathbf{x}, t) - \bar{W}_i^{eq}(\mathbf{x}, t)) \end{aligned}$$

where  $S_i = -(\Theta[V]\bar{W})_i$  and  $\bar{W}^{eq}$  is an artificial “equilibrium” distribution such that  $\Pi(\bar{W}^{eq})_{\alpha_1, \alpha_1, \dots, \alpha_n}^n = \Pi(\bar{W})_{\alpha_1, \alpha_1, \dots, \alpha_n}^n$  for  $n \leq N_{\Pi}$ .  $\tau_w > 0$  and  $N_{\Pi} \in \mathbb{N}$  are model parameters. *It is interesting to observe that a formal approach to derive Eq. (14) similar to that presented in Ref.[38] for the Lattice Boltzmann equation may be possible.*

Compared to Eq.(13), Eq.(14) exhibits two additional terms. The last one eliminates first-order discretization artifacts [39, 40], while the first,  $\Omega_i$ , is a regularizing artificial collision term. Since  $\Omega$  is a relaxation-type collision term, its use is allowed because it preserves the positive semidefinite character of the density matrix that underlies the Wigner function [6, 41]. Its role is to improve the stability of the numerical scheme by inducing selective numerical dissipation without directly affecting the dynamics of the first  $n \leq N_{\Pi}$  moments of the Wigner equation. This can be seen as follows, let us consider the Taylor expansion up to second order of Eq.(14), namely

$$D_i\bar{W}_i + \frac{\delta t}{2}D_i^2\bar{W}_i = \Omega + S_i + \frac{1}{2}\left(\delta tD_iS_i - \frac{\delta t^2}{2}D_i^2S_i\right), \quad (15)$$

By solving for  $D_i\bar{W}_i$  and recursively substituting back in the second term of the l.h.s of Eq.(15), it is found that

$$\begin{aligned} D_i\bar{W}_i + \\ \frac{\delta t}{2}D_i\left(-\frac{\delta t}{2}D_i^2\bar{W}_i + \Omega + S_i + \frac{1}{2}\left(\delta tD_iS_i - \frac{\delta t^2}{2}D_i^2S_i\right)\right) &= \\ \Omega + S_i + \frac{1}{2}\left(\delta tD_iS_i - \frac{\delta t^2}{2}D_i^2S_i\right). & \quad (16) \end{aligned}$$

From Eq.(16), it can be seen that had the *last term of Eq. (14)* not been introduced in the definition of the

model, there would be an uncompensated [source dependent](#) term of order  $\delta t$ . Finally, if the velocity moments of Eq.(16) are calculated, it can be seen that all the contributions involving  $\Omega_i$  vanish, provided that the order of the moment is not larger than  $N_\Pi$ . Thus, up to terms of order  $O(\delta t^2)$  and  $n \leq N_\Pi$ , the resulting set of equations

$$\begin{aligned} \frac{\partial}{\partial t} \Pi(\bar{W})_{\alpha_1, \alpha_1, \dots, \alpha_n}^n + \nabla \cdot \Pi(\bar{W})_{\alpha_1, \alpha_1, \dots, \alpha_{n+1}}^{n+1} \\ = \Pi(\bar{S})_{\alpha_1, \alpha_1, \dots, \alpha_n}^n + O(\delta t^2), \end{aligned} \quad (17)$$

is consistent, with the moments of Eq.(9).

In summary, Eq.(14) approximately solves the Wigner Equation by solving the corresponding truncated hierarchy of equations Eq.(17).

To finalise the model description, a quadrature  $\{\mathbf{v}_i, w_i\}_{i=1}^{N_q}$  and the explicit expressions for  $\bar{W}_i$ ,  $S_i$  and  $\bar{W}_i^{eq}$  are needed. Since the Wigner function is bounded over the phase space [42] and only a limited number of moments are required, due to the truncation in Eq. (17), an expansion in orthonormal polynomials can be assumed for  $\bar{W}$ ,  $S$  and  $\bar{W}^{eq}$ , from which the expressions of the corresponding distributions can be derived.

For instance, given a family of polynomials  $\{P_n(\mathbf{v})\}$ , orthonormal under the weight function  $\omega(\mathbf{v})$ ,  $\bar{W}$  can be represented approximately as:

$$\bar{W}(\mathbf{x}, \mathbf{v}, t) \approx \omega(\mathbf{v}) \sum_n^{N_p} a_n(\mathbf{x}, t) P_n(\mathbf{v}), \quad (18)$$

where  $N_p$  is the maximum order of the polynomials used in the representation and the expansion coefficients are given by

$$a_n(\mathbf{x}, t) = \int d^3\mathbf{v} \bar{W}(\mathbf{x}, \mathbf{v}, t) P_n(\mathbf{v}). \quad (19)$$

It is interesting to note that, since the expansion coefficients are linear combinations of the moments of the distribution, this procedure is similar to Grad's method[43], although not restricted to Hermite polynomials.

Since any combination of the form  $v_{i\alpha_1} v_{i\alpha_1} \dots v_{i\alpha_n}$  can be represented exactly using the set  $\{P_n(\mathbf{v})\}$ , the requirement of Eq.(12) is equivalent to solving the following set of algebraic constraints:

$$\begin{aligned} \sum_{i=0}^{N_q} \omega_i P_n(\mathbf{v}_i) P_m(\mathbf{v}_i) &= \delta_{n,m} \quad \forall n, m \leq N_p \\ \mathbf{v}_i &\in \mathbb{Z}^d \quad \forall i \\ w_i &\geq 0 \quad \forall i, \end{aligned} \quad (20)$$

for  $\mathbf{v}_i, w_i$ .

Technically the constraint  $\mathbf{v}_i \in \mathbb{Z}^d$  is not necessary. However, without such constraint, a interpolation would be needed whenever  $\mathbf{x} + \mathbf{v}_i \delta t$  fails to fall on spatial lattice. Finally, following a consolidated convention, quadratures in  $n$  spatial dimensions with  $m$  discrete velocity vectors will be designated by  $DnQm$ .

Given a solution of Eq.(20)  $\bar{W}_i$  can be expressed as

$$\bar{W}_i(\mathbf{x}, t) = \omega_i \sum_n^{N_p} a_n(\mathbf{x}, t) P_n(\mathbf{v}_i), \quad (21)$$

and similarly for  $S_i$  and  $\bar{W}_i^{eq}$ .

In practice, Hermite polynomials are a convenient choice, as they permit the systematic generation of lattices in any number of dimensions [44–46]. For example, in one dimension and using Hermite polynomials,  $\mathcal{H}_n(v; c_s)$  with weight function  $\omega(v; c_s) = \frac{1}{\sqrt{2\pi c_s^2}} e^{-\frac{v^2}{2c_s^2}}$  and parameter  $c_s > 0$  [47], the expressions for  $\bar{W}_i$ ,  $S_i$  and  $\bar{W}_i^{eq}$  are given by

$$\bar{W}_i = \omega_i \sum_n^{N_p} a_n(x, t) \mathcal{H}_n(v_i; c_s) \quad (22)$$

$$\bar{W}_i^{eq} = \omega_i \sum_n^{N_\Pi} a_n(x, t) \mathcal{H}_n(v_i; c_s) \quad (23)$$

$$S_i = -\omega_i \sum_{n,s} a_n(x, t) \sqrt{\frac{(n+s)!}{n!}} \frac{(-H/i)^{s-1}}{c_s^s s!} \frac{\partial^s V}{\partial x^s} \mathcal{H}_{n+s}(v_i; c_s). \quad (24)$$

Where  $H$  is the dimensionless reduced Planck constant. It should be noted that, in general, the condition  $N_\Pi < N_p$  must hold, for otherwise  $\Omega_i$  becomes trivially zero. [\(For algorithmic details see appendix B\)](#)

Throughout this work Hermite polynomials are in use as they naturally fit the considered problems. However, other choices adapted to particular problems are possible. An example of this, are the generalized polynomials for electronic problems developed in [48].

## IV. VALIDATION

We validate our model, first for the harmonic oscillator and then for the case of anharmonic potentials with up to sixth order.

### A. Harmonic potential

As a first example to illustrate the lattice Wigner method described in the previous sections, we consider the quantum harmonic oscillator described by the following Hamiltonian Eq. (25):

$$\hat{H} = \frac{\hat{p}^2}{2} + \frac{1}{2} \hat{x}^2. \quad (25)$$

We track the time propagation of the  $\bar{W}_i$  distributions from the initial conditions, for different choices of the spatial resolution and number of moments  $N_\Pi$ .

The initial condition consists of an equally weighted superposition of the first two eigenstates of the quantum

harmonic oscillator,  $|\phi\rangle = \frac{1}{\sqrt{2}}(|\psi_0\rangle + |\psi_1\rangle)$ . Since this state is non stationary, it shows time oscillations all along the evolution.

The Wigner function corresponding to  $|\phi\rangle$  can be calculated from the definition Eq.(1), the result being:

$$W_{|\phi\rangle}(x, v) = \frac{e^{-\frac{v^2 + x^2}{H}}}{\pi H^2}. \quad (26)$$

Observe that if Hermite polynomials are used,  $W_{|\phi\rangle}(x, v)$  is already of the form Eq.(18). It follows that the distributions,  $\bar{W}_i$ , are given by

$$\bar{W}_i = \omega_i \frac{e^{-\frac{x^2}{2c_s^2}}}{\sqrt{2\pi c_s^2}} \left( \frac{\mathcal{H}_2(v_i; c_s)}{2} + \frac{c_s^2 + 2c_s x + x^2}{\sqrt{2}c_s^2} \mathcal{H}_1(v_i; c_s) \right) \quad (27)$$

where the specific values of  $w_i$ ,  $v_i$  and  $c_s$  for different lattices are given in the Appendix A and  $H$  was taken to be numerically equal to  $2c_s^2$ .

The results of our simulation using the D1Q3 lattice with a lattice spacing  $\delta x = 0.06$  and a equilibrium function with  $N_\Pi = 3$ , are shown in Fig. 1. On the upper panel, it can be seen that both the zeroth and first order moments ( $\rho, \rho u$ ) are correctly propagated and agree with the theoretical values at different times.

From Eq. (18), it is clear that, given the expansion coefficients  $a_n(\mathbf{x}, t)$ , it is possible to reconstruct an approximation of the Wigner function. These coefficients can be obtained from Eq.(22) as linear combinations of the moments of the Wigner function, which, in turn, can be calculated by means of quadratures.

The results for the quantum harmonic oscillator are presented on the lower panel of Fig.1, which shows the phase-space representation of the Wigner function. From this figure, a prototypical shape is clearly recognized, including the expected nonclassical regions of negative values.

To quantitatively characterize the present method, we have studied the effects of the spatial resolution, lattice configuration and number of preserved moments ( $N_\Pi$ )

To this end, the root mean square error between the theoretical density and the simulated one after a full oscillator period,  $T_0$ ,

$$\Delta = \sqrt{\frac{1}{N_x} \sum_x (\rho_{theory}(x) - \rho_{sim}(x))^2}, \quad (28)$$

was evaluated for different conditions.

In Fig.2 a), the effect of using different lattices and resolution levels is shown; two features are apparent, namely that the error  $\Delta$  decreases quadratically as a function of  $1/\delta x$  and that, at a given value of the resolution  $\delta x$ , schemes with higher number of preserved moment provide better results.

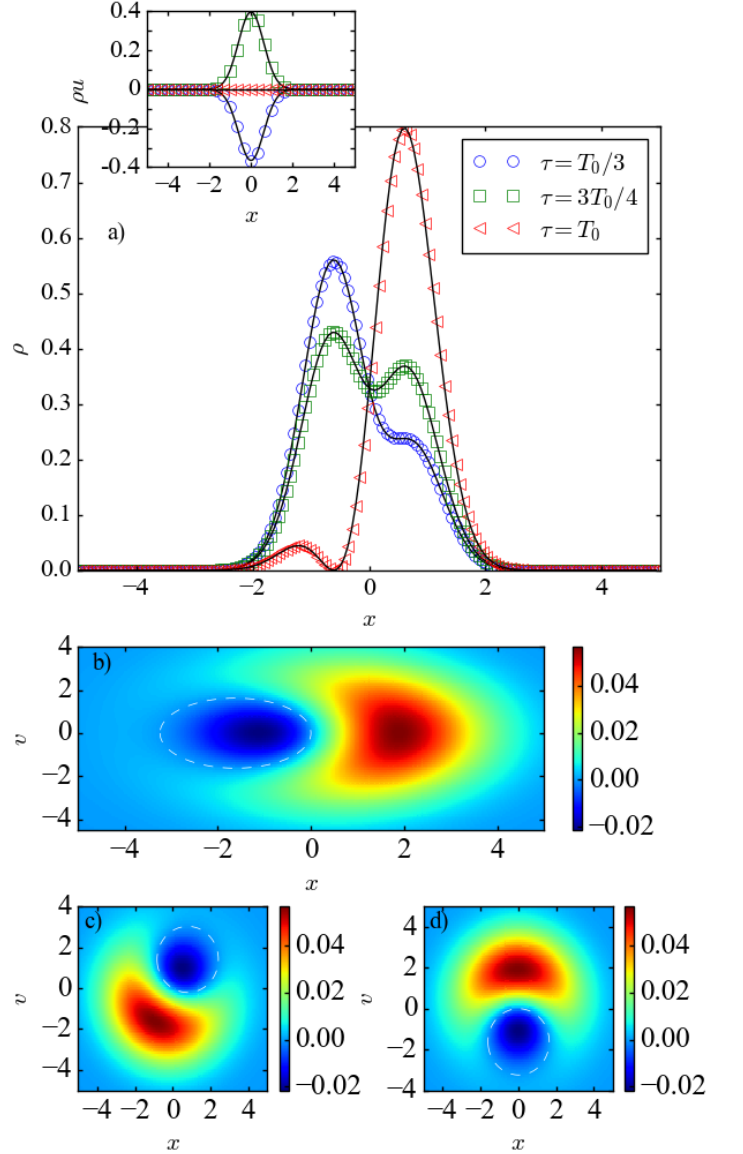


FIG. 1. (Color on line) a) First moment of the Wigner function (density) for different times being fractions of the oscillation period  $T_0$ . The inset shows the corresponding time evolution for the second moment (velocity density). The symbols denote the simulation and the solid lines the analytical solution. b) Phase space reconstruction of the quantum harmonic oscillator Wigner function at  $\tau = T_0$ . The dashed contour line shows where the Wigner function vanishes. c,d) Show the rotation of the harmonic Wigner function for  $\tau = T_0/3$  and  $\tau = T_0/4$  that is expected from the theory.

The effect of changing the value of  $N_\Pi$  is presented in Fig.2 b). From this figure, an ideal range for  $N_\Pi$  can be identified. If  $N_\Pi$  is low, the order of truncation of Eq.(17) leads to a crude approximation which in turn yields large values of  $\Delta$ . On the other end, if  $N_\Pi$  is equal to  $N_p$ , the model becomes unstable (this is why we have chosen  $N_\Pi < N_p$  for both lattices), because then the collision



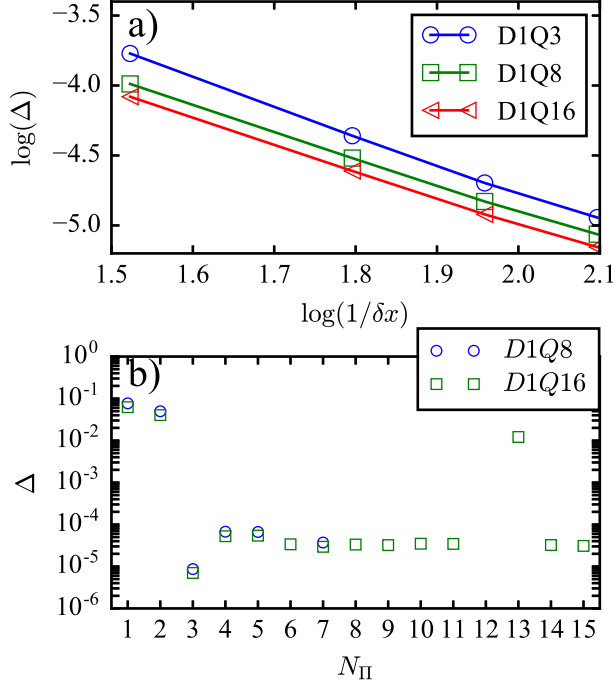


FIG. 2. (Color online) a) Root mean square error of the density,  $\Delta$ , for different velocity lattices and spatial resolution using an equilibrium function that preserves the first three moments. b) Effect on  $\Delta$  of using different values of  $N_\Pi$  for two different lattices with  $\delta x = 0.008$ ,  $N_p = 8$  and  $N_p = 16$  for D1Q8 and D1Q16 respectively.

term  $\Omega_i$ , Eq.(14), vanishes, which implies no artificial dissipation, hence the onset of stability issues discussed in Ref.[34]. The anomalous point  $N_\Pi = 13$ , in the D1Q16 case on Fig.2 b), may be due to compensated high order modes that reduce the artificial dissipation leading to a larger than expected error. That was only observed for the particular case of the harmonic oscillator (and wont be the case for the anharmonic potential).

### B. Anharmonic potential

As a second example, we simulate the anharmonic quantum oscillator described by the Hamiltonian

$$\hat{H} = \frac{\hat{p}^2}{2} + \frac{1}{2}\hat{x}^2 + \alpha\hat{x}^4 + \beta\hat{x}^6, \quad (29)$$

where the parameters  $\alpha$  and  $\beta$  determine the strength of the anharmonic terms.

As discussed earlier on, anharmonic terms involve genuinely quantum effects in the forcing expansion described in Eq. (8).

Similar to the previous example, the initial condition is taken to be the equal superposition of the first two eigenstates of the hamiltonian Eq.(29)  $|\phi\rangle = \frac{1}{\sqrt{2}}(|\psi_0\rangle + |\psi_1\rangle)$ . Here,  $|\psi_0\rangle, |\psi_1\rangle$  are obtained by direct diagonalization of

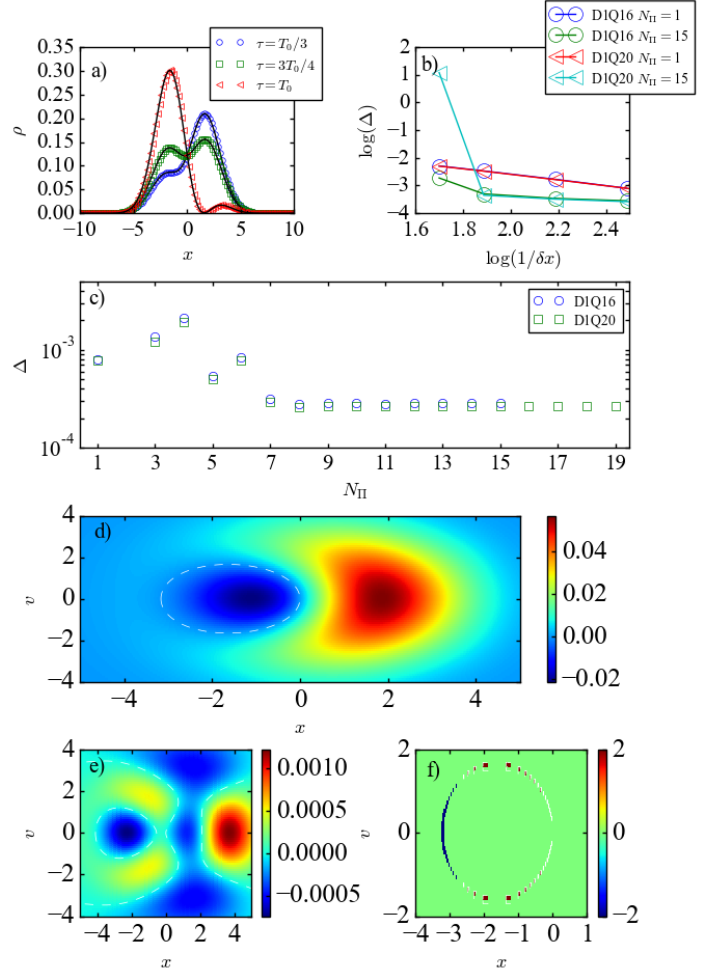


FIG. 3. (Color online) Results for the anharmonic oscillator with parameters  $\alpha = 0.1$ ,  $\beta = 0.05$ . a) Comparison between the density obtained using the Lattice Wigner method and the one obtained directly from the Schrödinger equation. (b) Error as a function of resolution, used lattice and number of projections  $N_\Pi$ . It can be seen that as the resolution increases the error saturates and that the error decreases upon increasing the number of projections. (c) Effect on  $\Delta$  of using different values of  $N_\Pi$  for two different lattices with  $\delta x = 0.008$ . (d) Reconstruction of the Wigner function from the anharmonic case, the dashed contour line shows the region where the Wigner function vanishes (e) Difference between the harmonic and anharmonic Wigner functions in phase space. (f) Difference between the signs of the harmonic and anharmonic Wigner functions. A value of +2 indicates a region where the harmonic Wigner function is positive and the anharmonic is negative, -2 indicates the opposite situation.

Eq. (29), using a truncated basis set of 50 eigenvectors,  $\varphi_n$ , from the quantum harmonic oscillator.

The density matrix for this system is given by  $\hat{\rho}(x, x') = \sum_{m,n} c_n c_m^* \varphi_m(x) \varphi_n(x')$ , where the coefficients  $c_n$  are easily obtained from the diagonalization procedure. Given  $\hat{\rho}$ , the corresponding Wigner function  $W_{|\phi\rangle}(x, v)$  was calculated with the help of the results in

Ref. [49], leading to the following expression:

$$W_{|\phi\rangle}(x, v) = \frac{1}{2\pi H} \sum_{n \leq m} \frac{2}{1 + \delta_{m,n}} \Re(c_n c_m^* k_{n,m}), \quad (30)$$

where  $\Re(\cdot)$  denotes the real part, the coefficients  $k_{m,n}$  are given by

$$k_{m,n} = 2(-1)^{\min(m,n)} \sqrt{\frac{\min(m,n)!}{\max(m,n)!}} e^{-\frac{x^2+v^2}{H}} \left( \frac{2}{H}(x^2+v^2) \right)^{\frac{|m-n|}{2}} L_{\min(m,n)}^{|m-n|} \left( \frac{2}{H}(x^2+v^2) \right) e^{i(m-n) \arctan(v/x)} \quad (31)$$

and  $L_n^m$  is the  $m$  order  $n$  degree associated Laguerre polynomial.

In order to find the corresponding  $\bar{W}_i$ , the fact is used that each term of Eq. (30) can be written as the product of a polynomial and a Gaussian function in the velocity space. Once the Gaussian is factored out, the result in Eq. (32) is readily cast into the form of Eq. (18), namely

$$W(x, v) = \frac{e^{-\frac{v^2}{H}}}{\sqrt{2\pi H}} \sum_{n \leq m} \frac{2}{1 + \delta_{m,n}} (c_{nm}^r \bar{k}_{nm}^r - c_{nm}^i \bar{k}_{nm}^i), \quad (32)$$

In the above,  $c_{nm} = (c_n^r c_m^r + c_n^i c_m^i) + i(c_n^i c_m^r - c_m^i c_n^r)$  and  $\bar{k}_{mn} = \frac{e^{v^2/H}}{2\sqrt{\pi H}} k_{mn}$ , where the superscripts  $r$  and  $i$  denote real and imaginary parts, respectively. Since Hermite quadratures are in use, the  $\bar{W}_i$  follow directly.

The results for the anharmonic oscillator Eq.(29) with parameters  $\alpha = 0.1$ ,  $\beta = 0.05$  are summarized in Fig.3 a), from which it is apparent that for mild anharmonicities, the method is able to properly evolve the given initial condition. In Fig.3 b) the error as a function of the used lattice and resolution is reported; the general trend is an error decrease at increasing resolution; it decreases as  $N_\Pi$  increases and  $\Delta$  tends to saturate relatively fast. In Fig.3 c), the behavior of  $\Delta$  as function of  $N_\Pi$  is shown. Similarly to the harmonic case, as  $N_\Pi$  increases,  $\Delta$  decreases, until it reaches and optimal value ( $N_\Pi = 8$ ) and then saturates.

The Wigner function  $\bar{W}^{anh}$  was also reconstructed for the anharmonic oscillator Fig. 3 d). To observe the quantitative difference between it and the Wigner function of the harmonic oscillator  $\bar{W}^h$ , the difference  $\bar{W}^h - \bar{W}^{anh}$  is shown in Fig. 3 e). Finally it is interesting to notice that for the given levels of anharmonicity the change in the negative region of the Wigner function concentrates on the boundary of the negative region this is shown in Fig. 3 f) where the sign difference  $\text{sgn}(\bar{W}^h) - \text{sgn}(\bar{W}^{anh})$  is plotted.

In order to study stronger anharmonic cases, not only larger resolutions, but also more terms in the representation Eq.(22) of the Wigner function are required because as the strength of the anharmonicity increases, so does

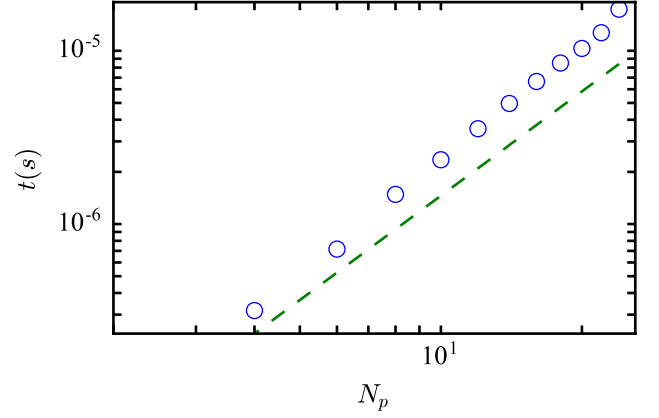


FIG. 4. (Color online) The symbols show the time it takes to update a single site as a function of the number of polynomials. The dashed line shows the scaling  $t \sim N_p^2$ . The simulations were performed for the quantum harmonic oscillator, in every case  $N_\Pi$  was set to the highest value compatible with numerical stability.

the number of terms in Eq.(32). In order to account for them, both the number of polynomials in Eq.(22) and the size of the velocity lattice needs to be increased.

The effect of the relaxation time of  $\tau_w$  was also studied. By definition, this parameter controls dissipative effects and consequently, it is not expected to affect the results. However, numerically it was found that this is the case only in the range  $0.56 \leq \tau_w \leq 5$ , which is similar to the allowed range of  $\tau_w$  in the closely related lattice Boltzmann schemes. This is possibly due to a marginal coupling between high order moments and the ones relevant to the Wigner dynamics.

### C. Computational cost

For an arbitrary problem, it is a priori not known how many polynomials are required to give an accurate representation of the Wigner function, Eq. (18). However, similarly to the classical Lattice Boltzmann methods, it is expected that in practice the number of terms in Eq. (18) can be minimized if the expected macroscopic velocities  $\bar{v} = |\Pi^1(\bar{W})/\Pi^0(\bar{W})|$  are much smaller than the Lattice speed of sound i.e  $|\frac{\bar{v}}{C_s}| \ll 1$ , and if the expansion Eq. (24) can be truncated on the basis that  $|H^{s-1} \partial_x^s \bar{v}| \ll 1$  for certain  $s$ . The number of polynomials,  $N_p$ , determines the smallest lattice that is able to support the orthogonality constraints, Eq. (20), and also the computational cost of solving the respective problem. The scaling of the cost can be estimated by observing that a single update of the complete set of lattice points involves four basic steps: 1) the calculation of the expansion coefficients  $a_n$  in Eq. (22), 2) the update of the source term distributions in Eq. (24), 3) the update of  $\bar{W}^{eq}$  in Eq. (21), and 4) the update of  $\bar{W}_i$  according to Eq.(14).

The number of floating point operations (+, −, ×, /) required at each step scales respectively as  $O(N_p N_q)$ ,  $O(N_s N_p N_q)$ ,  $O(N_p N_q)$  and  $O(1)$ , where  $N_s$  is the number of terms in Eq. (24) that are consistent with a cutoff at  $s$  in  $H$ .

Under a worst-case scenario, i.e. the largest possible  $N_\Pi$ ,  $N_\Pi \sim N_p$  and  $N_q \sim N_p$ , the total cost of updating a single site scales as:

$$O(N_s N_p^2 + N_p^2) \quad (33)$$

In 1D,  $N_s$  is effectively  $O(1)$  and therefore the cost per site update scales as  $O(N_p^2)$ . This bound was tested and the corresponding results are reported in Fig. 4, from which it is seen that the cost of updating a single site scales like  $N_p^2$ . The difference with respect to the theoretical value can be accounted for by the time to access data, which becomes dominant as the size of the problem is increased.

In 2D,  $N_s$  scales  $O(s^2)$ , and since the number of polynomials and lattice vectors also scale quadratically, the update cost per site is expected to grow as  $O(s^2 N_p^4)$ . For the 3D case  $N_s$  scales as  $O(s^3)$  and therefore the expected update cost per site is expected to grow as  $O(s^3 N_p^6)$ .

For comparison, the spectral and semispectral methods reported in Ref. [8, 34] scale in 1D as  $O(N \log N)$  where  $N$  is the number of basis functions. However, this only applies when plane wave basis are used, which are known to introduce numerical artefacts. If an arbitrary basis is used the reported scaling of Ref. [34] becomes  $O(N^2)$ . Finally it is interesting to note that Ref. [22] reports  $O(N \log N)$  complexity for 2 particles in a single dimension using Fourier methods.

## V. DRIVEN OPEN QUANTUM SYSTEMS

### A. 1D system

As an application of the proposed model, next we study the dynamics of the zeroth and first moment of the Wigner function for a system subject to the combined action of an external drive and potential barriers. As a model of an homogeneous system, we assume that the initial state is given by the following thermal density matrix:

$$\hat{\rho} = \sum |p\rangle \langle p| e^{-\beta p^2/2m}, \quad (34)$$

where  $|p\rangle$  are plane waves,  $m$  is the mass of the particle and  $\beta$  is the inverse temperature.

The system is taken to be of finite length  $L$ , which implies quantization of the allowed momenta. However,  $L$  is assumed sufficiently large to justify a continuum limit.

The potential barriers extend throughout the domain according to:

$$V(x) = \frac{v_0}{2} (\text{erf}((x + \delta/2)\xi) - \text{erf}((x - \delta/2)\xi)), \quad (35)$$

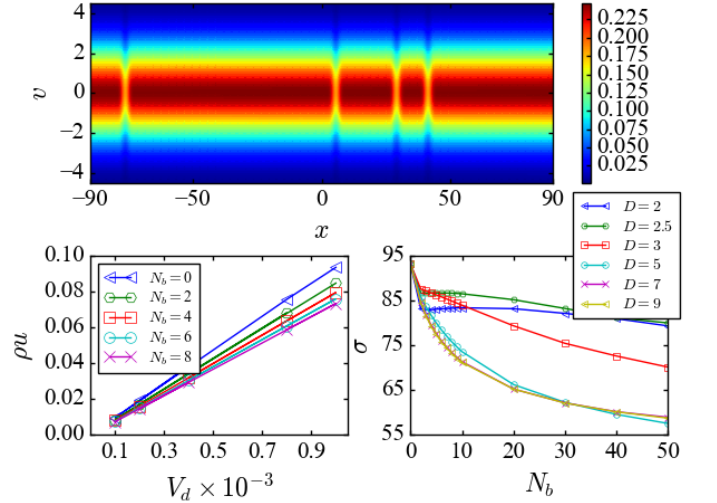


FIG. 5. (Color online) a): Reconstructed steady state Wigner function. b): The second moment of the Wigner function as function of  $V_d$  in steady state, for different number of barriers  $N_b$ . c)  $\sigma$  as a function of the number of barriers for different inter barrier distances. The system size is set to 400 (in dimensionless units) and all simulations were performed with a resolution  $\delta x = 0.004$ , with  $N_\Pi = 14$ , using a D1Q16 lattice.

where  $v_0$ ,  $\delta$  and  $\xi$  define the height, width and stiffness of the barrier, respectively. The barriers were symmetrically distributed at the points  $\{x_i = \pm Di\}$ ,  $i = 0, 1, \dots, N_b$  where  $D$  is the interbarrier distance.

The system is driven by the potential  $V_d(x) = -ax$ , where  $a$  determines the strength of the forcing, and is assumed to be open, i.e. each end of the domain is connected to a fixed reservoir, also described by Eq. (34).

Similar to the previous examples, a lattice Wigner representation of the form Eq. (21) is required for the initial condition. In this case, the Wigner transform of Eq. (34) is given by

$$W(x, v) = \frac{1}{2\pi H} e^{-\frac{v^2 \bar{\beta}}{2}}, \quad (36)$$

where  $\bar{\beta} = \beta m (l_0/t_0)^2$ .

Comparing Eq.(36) with the form of the Hermite polynomials weight function,  $\omega(v; c_s) = \frac{1}{\sqrt{2\pi c_s^2}} e^{-\frac{v^2}{2c_s^2}}$ , and using Eq.(18,21) it follows that if  $\bar{\beta}$  and  $H$  are fixed respectively to  $1/c_s^2$  and  $c_s$  then only the  $a_0$  expansion coefficient, that correspond to the constant Hermite polynomial, is required. That is, the representation of the initial condition is optimal and the distributions  $\bar{W}_i$  are proportional to the weights of the lattice configuration

$$\bar{W}_i = \omega_i \frac{1}{\sqrt{2\pi}}. \quad (37)$$

Finally, it is important to observe that the barrier potential Eq. (35) has infinitely many non-zero derivatives,



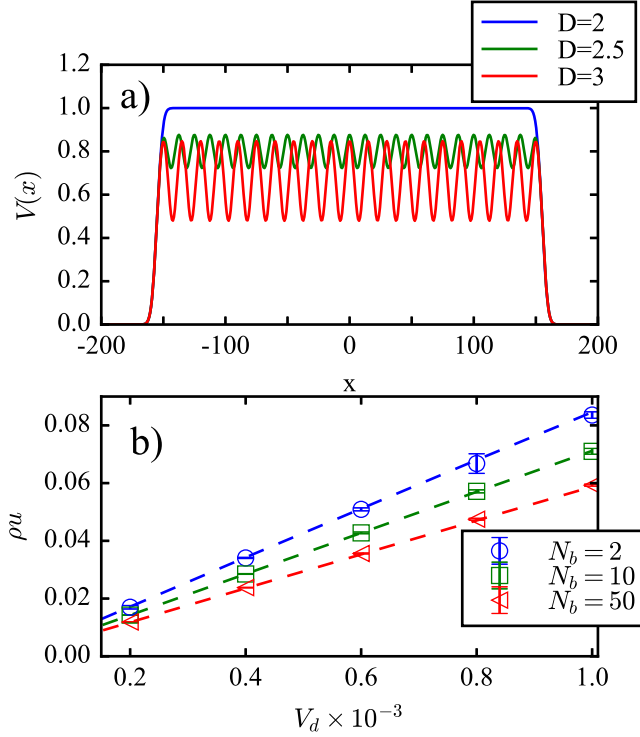


FIG. 6. (Color online) a) The total potential as a function of the inter barrier separation. For  $D = 2$  the barriers are close enough such that the total resulting potential acts as a single barrier. As the interbarrier separation increases, the resulting potential exhibits the structure shown for the  $D = \{2.5, 3\}$  cases b) The symbols show the behavior of  $\rho u$ , averaged over 50 random samples, as a function of the driving potential. The dashed lines show the behavior of  $\rho u$  in the uniformly distributed case with an inter barrier distance  $D = 8$ .

as opposed to the harmonic and anharmonic potentials. This implies that a cutoff in Eq. (24) needs to be chosen. For the present simulations, the parameters characterising the barriers were fixed as  $v_0 = 0.4\beta^{-1}$ ,  $\delta = 2$  and  $\xi = 1$ . In this case, the cutoff is taken at  $s = 9$ , since the next contribution,  $s = 11$ , is six orders of magnitude smaller than the first order contribution.

The first two moments of the Wigner function were studied for different values of the driving force  $V_d$ , number and location of the barriers. Fig. 5 a) shows the reconstructed steady state Wigner function,  $\bar{W}(x, v)$ , of a system with  $V_d = 10^{-4}$  and four barriers randomly located across the domain.

Similar results were obtained for different configurations of barriers and driving force. The first visible feature is that  $\bar{W}(x, v)$  shows a number of “cuts” along the  $v$  axis at given values of  $x$ . These cuts are located at the potential barriers. Along the barriers, the Wigner function attains lower values as compared to the nearby regions. This implies that the density in the cuts is smaller compared to the surroundings.

A second feature is that the Wigner function is nearly

translationally invariant in the interstitial region between two subsequent cuts, as long as the cuts are sufficiently far apart, which implies that the density  $\rho$  is uniform between cuts.

Further, from Fig. 5 a) it seems that the Wigner distribution is symmetric along the  $v = 0$  axis, although this is not the case. The driving potential slightly shifts the distribution, leading to a finite and spatially uniform first moment ( $\rho u$ ), which is consistent with the continuity equation  $\frac{\partial \rho}{\partial t} + \nabla \rho u = 0$ , at steady state. Finally, it can be seen that the Wigner function is nowhere negative, first, because the reservoir naturally tends to wash out quantum coherence and second, because the ratio between the height of the barriers and the thermal energy is about 0.4, whereas in applications such as resonant tunneling diodes, such ratio is about ten [18]. Similarly to the case of strong anharmonicities, to treat systems with higher energy barriers, more terms i.e. polynomials in the representation of the Wigner function (Eq.(18)) are needed, along with the corresponding increase in the velocity lattice size. For instance, in the case of a resonant tunnelling diode, preliminary simulations showed that velocity lattices as large as  $D1Q77$  where not able to recover the negative regions of the system. It is expected that by using polynomials adapted to the problem the system can be approached in the future

From Fig. 5 b) it can be seen that the relation between the velocity density  $\rho u$  and the forcing potential  $V_d$  is linear for a fixed number of barriers, uniformly and symmetrically distributed across the domain. Further, Fig. 5 b) also implies that, as the number of barriers increases, the electric conductivity,  $\sigma$ , decreases.

In other terms, the capacity of the system to transport momentum from one end to the other, declines with number of barriers. To quantify this relation, simulations with a fixed number of barriers,  $N_b$ , but different inter-barrier distances,  $D$ , were performed. The results, reported in Fig.5 c), show that the overall tendency is a decreasing  $\sigma$  at increasing  $N_b$ . However, this decrease shows a dependence on the inter-barrier separation  $D$ . For  $D = 2$  and  $D = 2.5$ ,  $\sigma$  is nearly constant, whereas for  $D \geq 3$  it decreases rapidly with  $N_b$ . Furthermore,  $\sigma$  saturates above  $D \geq 5$ .

The above picture can be understood as follows: once the barriers are sufficiently close together, they overlap and the resulting potential is no longer a set of disjoint barriers, but rather a single larger barrier Fig.6 a).

In this case, it is known that all incoming plane waves with energy below the barrier are exponentially attenuated as a function of the barrier length, whereas those with energy above the barrier manage to penetrate, if only with a non-zero reflection probability. It follows then that the number of states that can cross the barrier diminishes as the length of the barrier increases thereby limiting the amount of momentum transported across the system, thus leading to an overall decrease of  $\sigma$ .

When the separation between the barriers is sufficiently large, the system can be approximated as a se-

$D$	$a$	$b$	$c$
5	$29.1 \pm 0.6$	$59.5 \pm 0.5$	$0.913 \pm 0.005$
5.5	$28.7 \pm 0.7$	$59.7 \pm 0.5$	$0.912 \pm 0.005$
6	$28.7 \pm 0.7$	$59.6 \pm 0.5$	$0.913 \pm 0.005$
6.5	$28.8 \pm 0.7$	$59.5 \pm 0.5$	$0.914 \pm 0.005$
8	$28.9 \pm 0.7$	$59.4 \pm 0.5$	$0.914 \pm 0.005$

TABLE II. Individual fitting parameters of Eq.(38) for different interbarrier distances

quence of disjoint barriers. If the system was closed, this would imply that,  $T$  being the transmission coefficient for a single incoming plane-wave on a single barrier, the transmission coefficient for  $n$  barriers, would be  $T^n$ , without any dependence on the inter barrier separation. Since this holds for every plane wave contributing to the thermal density matrix, the system as a whole is expected to follow a similar trend.

From the previous picture, it can be inferred that the  $\sigma - n$  relation must have a similar form for the  $D \geq 5$  settings. The semi empirical formula  $\sigma = a + bc^n$ , where  $a, b, c$  are parameters depending on the inter-barrier separation, offers a good fit to the cases  $D = 5, 5.5, 6, 6.5, 8$ . From Table.V A, it is apparent that the parameters  $a, b$  and  $c$  are constant within error bars. Therefore, for  $D \geq 5$ , the relation between  $\sigma$  and  $n$  and  $D$ , is effectively independent of  $D$  and given by

$$\sigma = a + bc^n \quad (38)$$

with  $a = 28.8 \pm 0.1$ ,  $b = 59.5 \pm 0.1$ ,  $c = 0.913 \pm 0.001$ .

The intermediate case  $2.5 < D < 5$ , when the barriers do not form a single monolithic barrier and the system can no longer be regarded as a superposition of disjoint subsystems, requires a deeper analysis which is left for future work.

We have also studied the momentum transport in the presence of a random distribution of barriers.

Simulations were performed for a fixed number of barriers  $N_b$ , randomly located across the domain. The minimum distance between any two barriers was constrained to be larger than 2 lattice sites, in order to avoid excessive overlap, leading to an effective single larger barrier instead of two distinct ones. The results are presented in Fig. 6 b), where for every instance 50 random realisations were considered.

The main observation is that the relationship between the current  $\rho u$  and  $V_d$  is, on average, the same as with uniformly distributed barriers, with an inter-barrier distance  $D > 5$ . This result can be understood as follows; since the barriers are constrained to be far apart, most configurations behave as a collection of subsystems. This, in turn, implies that  $\sigma$  only depends on the number of barriers Eq.(38) and, as a consequence, the average relation between  $\rho u$  and  $V_d$  does not depart significantly from the case of a regular distribution of barriers.

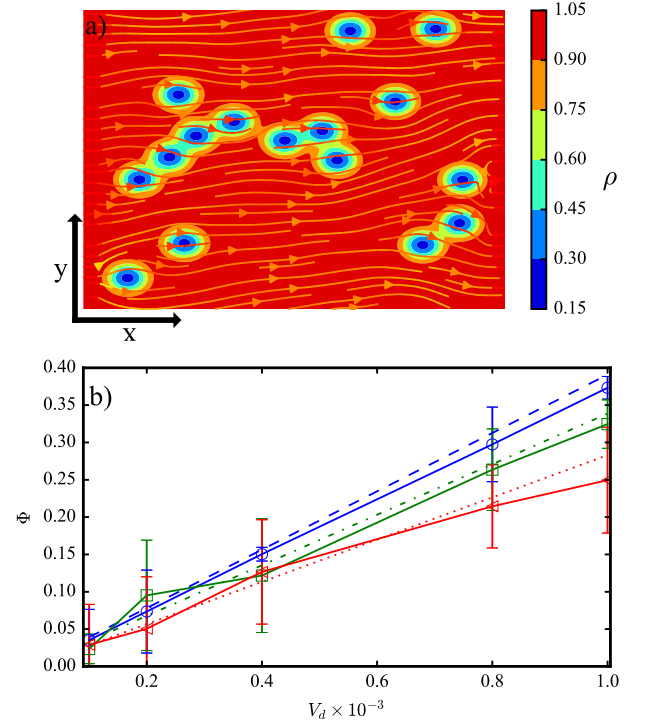


FIG. 7. (Color online) a) Density map for a 2D system with 16 randomly located barriers. The effect of the barriers can be observed on the regions that get depleted (blue color) and on the streamlines that bend around them. b) Behavior of  $\Phi$  as a function of the driving strength. The red dashed line, blue dot-dashed line and green dotted line correspond to systems where the barriers are arranged in regular grids of  $2 \times 2$ ,  $3 \times 3$  and  $4 \times 4$  barriers with an inter barrier distance of  $D = 9$ . The circle, square and triangle symbols represent respectively the mean flux of 50 random samples of  $2 \times 2$ ,  $3 \times 3$  and  $4 \times 4$  randomly located barriers. The solid lines are a guide to the eye showing the trend of  $\Phi$  as a function of  $V_d$  for the case of random barriers.

## B. 2D system

The transport properties of a square shaped two-dimensional system of side length  $L$ , were also studied. Open boundary conditions were used at the  $x = 0$  and  $x = L$  ends, while periodic boundary conditions are used at the  $y = 0$  and  $y = L$  ends. The system is driven by an external potential of the form  $V_d(\mathbf{x}) = -ax$ , where  $a$  controls the strength of the external driving. The barriers are described by the potential

$$V(\mathbf{x}) = v_0 e^{-\frac{|\mathbf{x}|^2}{2\xi^2}}, \quad (39)$$

where  $v_0$  determines the height of the barrier and  $\xi$  its stiffness.

The initial state is also given by Eq. (34), where  $|p\rangle$  is assumed to be two dimensional. Following calculations similar to the 1D case, the initial condition for the lattice

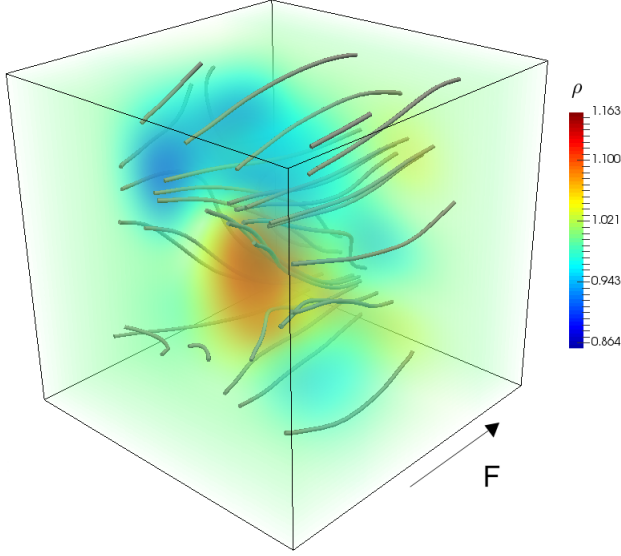


FIG. 8. (Color online) The figure shows the density  $\rho$  and streamlines of  $\rho\mathbf{u}$  of an open driven system in 3D. The drive is given by a constant force,  $F$ , along the  $\mathbf{x}$  direction.

Wigner model is given by

$$\bar{W}_i = \omega_i \frac{1}{2\pi}. \quad (40)$$

The cutoff of Eq.(10) was set to  $s = 9$  and the simulations were carried out on a  $256 \times 256$  grid, using the D2Q16 lattice (see Appendix for details).

Similarly to the 1D case, regular and a random settings for the location of the potential barriers were considered. Fig.7 a) shows a sample result for a simulation with 16 randomly placed barriers. The location of the potential barriers can be easily identified through the blue color spots, denoting density depletion. Further, it can be seen that the streamlines bend around the potential barriers, similarly to the way fluid streamlines turn around obstacles in porous or campylocytic media [50, 51].

The relation between the flux  $\Phi$  (2D analog of  $\rho u$  in 1D) and the driving potential is presented in Fig. 7 b). From this figure, it is seen that the relation  $\sigma$  versus  $\Phi$  and  $V_d$  is linear when the barriers are regularly organised on a square grid, and that  $\sigma$  decreases at increasing number of barriers. Furthermore, when the barriers are randomly placed, the average behavior of  $\Phi$  is close to the regular case, as it was also observed in 1D. However as the number of barriers increases, specific realizations can deviate significantly from the regular grid behavior, this can be seen from the error bars of the red triangles in Fig. 7 b).

Finally, for the purpose of showing the viability of the present method also in three spatial dimensions, we have simulated a three-dimensional open quantum system. The simulation was performed on a  $20 \times 20 \times 20$  lattice, with a D3Q125 velocity set, which was chosen

because it includes terms of order  $H^2$  in the force expansion Eq.(24). The boundary conditions are open (thermal density matrix) at the planes normal to  $F$  (See Fig.8) and periodic on the remaining boundaries. In addition to the driving potential generating a force in the  $x$  direction, a random potential is included. It is modeled as a smooth Gaussian with varying amplitude at different locations in the domain. From Fig.8, it is seen that the streamlines tend to circumvent the regions of low density, where the potential is high, and concentrate in the regions of high density, thus effectively avoiding “impurities”. A systematic analysis of the transport properties of this three-dimensional open quantum system is left for future work.

## VI. CONCLUSION

In this work, a new numerical method to track the time evolution of the Wigner function has been introduced. The stability problem previously described in Ref. [34], is handled through the inclusion of an artificial collision term, designed in such a way as to preserve the dynamics of the relevant moments of the Wigner function. The fact of reducing momentum space to a comparatively small set of representative momentum vectors, opens up interesting prospects for the simulation of one, two and also three dimensional quantum systems. Preliminary results for 1D systems with regular and random potentials provide evidence of linear transport laws which are independent of the barrier configuration for dilute systems. In the 2D case, we find the same transport laws at low barrier density, while for higher concentrations, deviations from the linear behavior are observed (as shown in Fig.7 b) when the barriers are randomly located. Finally, we also presented a preliminary simulation of a 3D open quantum system, to illustrate the ability of the model to handle the three-dimensional Wigner equation.

The computational cost of the method scales polynomially with the number of basis functions. However, the simulations show that just a few equilibrium moments and comparatively small lattices, are often sufficient to obtain reasonably accurate results.

The present work opens up a number of research directions for the future. Technically, the performance can be improved by choosing alternative families of lattice configurations and orthonormal polynomials, or by directly designing orthonormal polynomials that fit the specific problems under investigation. Since our model is computationally viable also in 3D, problems like the heat transport properties of three-dimensional semiconductor structures, which are highly relevant to the next generation electronics[52], could be studied. In addition, the method could also be used as a practical tool to explore fundamental issues, such as the relation between quantum entanglement and the Wigner function in diverse systems[53, 54] Or it could be adapted to directly study the time evolution of Hilbert space operators given the

relation between these and phase space operators via the Weyl transform.

## VII. ACKNOWLEDGMENTS

We acknowledge financial support from the European

Research Council (ERC) Advanced Grant No. 319968-FlowCCS.

- 
- [1] E. Wigner, *Phys. Rev.* **40**, 749 (1932).
  - [2] S. A. Gardiner, D. Jaksch, R. Dum, J. I. Cirac, and P. Zoller, *Phys. Rev. A* **62**, 023612 (2000).
  - [3] W. H. Zurek, *Nature* **412**, 712 (2001).
  - [4] M. A. Alonso, *Adv. Opt. Photon.* **3**, 272 (2011).
  - [5] D. Leibfried, T. Pfau, and C. Monroe, *Physics Today* **51**, 22 (1998).
  - [6] A. Jungel, *Transport Equations for Semiconductors* (Springer, Berlin-Heidelberg, 2009).
  - [7] W. R. Frensley, *Rev. Mod. Phys.* **62**, 745 (1990).
  - [8] C. Ringhofer, *SIAM Journal on Numerical Analysis* **27**, 32 (1990), <http://dx.doi.org/10.1137/0727003>.
  - [9] A. Arnold and C. Ringhofer, *SIAM Journal on Numerical Analysis* **32**, 1876 (1995), <http://dx.doi.org/10.1137/0732084>.
  - [10] T. Dittrich, C. Viviescas, and L. Sandoval, *Phys. Rev. Lett.* **96**, 070403 (2006).
  - [11] T. Dittrich, E. A. Gmez, and L. A. Pachn, *The Journal of Chemical Physics* **132**, 214102 (2010), <http://dx.doi.org/10.1063/1.3425881>.
  - [12] J. Sellier and I. Dimov, *Journal of Computational Physics* **270**, 265 (2014).
  - [13] J. Sellier and I. Dimov, *Journal of Computational Physics* **273**, 589 (2014).
  - [14] J. Sellier, M. Nedjalkov, and I. Dimov, *Physics Reports* **577**, 1 (2015), an Introduction to Applied Quantum Mechanics in the Wigner Monte Carlo Formalism.
  - [15] C. Jacoboni, R. Brunetti, P. Bordone, and A. Bertoni, *International Journal of High Speed Electronics and Systems* **11**, 387 (2001).
  - [16] K.-Y. Kim and B. Lee, *Solid-State Electronics* **43**, 2243 (1999).
  - [17] R. Mains and G. Haddad, *Journal of Computational Physics* **112**, 149 (1994).
  - [18] A. Dorda and F. Schrrer, *Journal of Computational Physics* **284**, 95 (2015).
  - [19] B. Niclot, P. Degond, and F. Poupaud, *Journal of Computational Physics* **78**, 313 (1988).
  - [20] C.-Y. Wong, *Journal of Optics B: Quantum and Semi-classical Optics* **5**, S420 (2003).
  - [21] V. S. Filinov, M. Bonitz, A. Filinov, and V. O. Golubnychiy, “Wigner function quantum molecular dynamics,” in *Computational Many-Particle Physics*, edited by H. Fehske, R. Schneider, and A. Weiße (Springer Berlin Heidelberg, Berlin, Heidelberg, 2008) pp. 41–60.
  - [22] R. Cabrera, D. I. Bondar, K. Jacobs, and H. A. Rabitz, *Phys. Rev. A* **92**, 042122 (2015).
  - [23] U. Frisch, B. Hasslacher, and Y. Pomeau, *Phys. Rev. Lett.* **56**, 1505 (1986).
  - [24] S. Wolfram, *Journal of Statistical Physics* **45**, 471 (1986).
  - [25] G. R. McNamara and G. Zanetti, *Phys. Rev. Lett.* **61**, 2332 (1988).
  - [26] R. Benzi, S. Succi, and M. Vergassola, *Physics Reports* **222**, 145 (1992).
  - [27] F. J. Higuera and S. Succi, *EPL (Europhysics Letters)* **8**, 517 (1989).
  - [28] S. Succi and R. Benzi, *Physica D: Nonlinear Phenomena* **69**, 327 (1993).
  - [29] M. Mendoza, S. Succi, and H. J. Herrmann, *Phys. Rev. Lett.* **113**, 096402 (2014).
  - [30] M. Mendoza, B. M. Boghosian, H. J. Herrmann, and S. Succi, *Phys. Rev. Lett.* **105**, 014502 (2010).
  - [31] M. Mendoza and J. D. Muñoz, *Phys. Rev. E* **82**, 056708 (2010).
  - [32] E. Ilseven and M. Mendoza, *Phys. Rev. E* **93**, 023303 (2016).
  - [33] S. Succi, *EPL (Europhysics Letters)* **109**, 50001 (2015).
  - [34] O. Furtmaier, S. Succi, and M. Mendoza, *Journal of Computational Physics* **305**, 1015 (2016).
  - [35] M. Hillery, R. O’Connell, M. Scully, and E. Wigner, *Physics Reports* **106**, 121 (1984).
  - [36] D. F. Styer, M. S. Balkin, K. M. Becker, M. R. Burns, C. E. Dudley, S. T. Forth, J. S. Gaumer, M. A. Kramer, D. C. Oertel, L. H. Park, M. T. Rinkoski, C. T. Smith, and T. D. Wotherspoon, *American Journal of Physics* **70**, 288 (2002), <http://dx.doi.org/10.1119/1.1445404>.
  - [37] S. P. Thampi, S. Ansumali, R. Adhikari, and S. Succi, *Journal of Computational Physics* **234**, 1 (2013).
  - [38] F. Bösch and I. V. Karlin, *Phys. Rev. Lett.* **111**, 090601 (2013).
  - [39] B. Shi, B. Deng, R. Du, and X. Chen, *Computers & Mathematics with Applications* **55**, 1568 (2008), mesoscopic Methods in Engineering and Science.
  - [40] J.-D. Debus, M. Mendoza, S. Succi, and H. J. Herrmann, *Phys. Rev. E* **93**, 043316 (2016).
  - [41] R. Rosati, F. Dolcini, R. C. Iotti, and F. Rossi, *Phys. Rev. B* **88**, 035401 (2013).
  - [42] W. B. Case, *American Journal of Physics* **76**, 937 (2008), <http://dx.doi.org/10.1119/1.2957889>.
  - [43] H. Grad, *Communications on Pure and Applied Mathematics* **2**, 331 (1949).
  - [44] S. S. Chikatamarla and I. V. Karlin, *Phys. Rev. Lett.* **97**, 190601 (2006).
  - [45] S. S. Chikatamarla and I. V. Karlin, *Phys. Rev. E* **79**, 046701 (2009).
  - [46] P. C. Philippi, L. A. Hegele, L. O. E. dos Santos, and R. Surmas, *Phys. Rev. E* **73**, 056702 (2006).
  - [47] M. M. Mizrahi, *Journal of Computational and Applied Mathematics* **1**, 273 (1975).
  - [48] Coelho, Rodrigo C. V., Ilha, Anderson S., and Doria, Mauro M., *EPL* **116**, 20001 (2016).
  - [49] H. Groenewold, *Physica* **12**, 405 (1946).
  - [50] M. Mendoza, S. Succi, and H. J. Herrmann, *Scientific Reports* **3**, 3106 EP (2013).

- [51] J. D. Debus, M. Mendoza, S. Succi, and H. J. Herrmann, *Scientific Reports* **7**, 42350 EP (2017).
- [52] W. Lu and C. M. Lieber, *Nat Mater* **6**, 841 (2007).
- [53] R. McConnell, H. Zhang, J. Hu, S. Cuk, and V. Vuletic, *Nature* **519**, 439 (2015).
- [54] N. Gonzalez, G. Molina-Terriza, and J. P. Torres, *Phys. Rev. A* **80**, 043804 (2009).
- [55] S. Succi, *The lattice Boltzmann equation: for fluid dynamics and beyond* (Oxford university press, 2001).



### Appendix A: Lattice specification

TABLE III. D1Q4 Lattice with  $c_s = 0.60625445810016454$ 

$\mathbf{v}_i$	$w_i$
0	0.63664690312607816284434609283846
-1,1	0.18141458774368577505004149208377
-3,3	0.00026196069327514352778546149699

TABLE IV. D1Q8 Lattice with  $c_s = 1.0658132602705641$ 

$\mathbf{v}_i$	$w_i$
0	0.37428019874212190129215011724318
-1,1	0.24105344284458452784844296921093
-2,2	0.06434304152476086575379872184362
-3,3	0.00713156628791277339406557854605
-4,4	0.00032523057375714836476726255033
-5,5	$6.6163470389851878681133911638949 \times 10^{-6}$
-7,7	$3.0508847488049822958363118638543 \times 10^{-9}$

TABLE V. D1Q10 Lattice with  $c_s = 1.229594448425497$ 

$\mathbf{v}_i$	$w_i$
0	0.32444899174631946866086595194671
-1,1	0.23309081165504033632566413700874
-2,2	0.08642582836940192624063184539752
-3,3	0.01653989847863324979993319254793
-4,4	0.00163342485156222352004541584861
-5,5	0.00008333063878279730921268566542
-6,6	$2.1783167706100240902344965225688 \times 10^{-6}$
-7,7	$3.1805869765623071575130276965860 \times 10^{-8}$
-9,9	$1.0779356826917937931616055896767 \times 10^{-11}$

2D lattices and in general  $n$  dimensional lattices can be constructed by taking  $n$  times the tensor product of the set of vectors and weights of a fixed 1D Lattice. For example, the D2Q4 lattice is given by Table.VIII. It is important to notice that this way of building higher dimensional lattices does not exhaust all possible lattices.

TABLE VI. D1Q16 Lattice with  $c_s = 1.6215048099592275$ 

$\mathbf{v}_i$	$w_i$
0	0.24603212869787232483785340883852
-1,1	0.20342468717937742901117526034797
-2,2	0.11498446042457243913866706495342
-3,3	0.04443225067964028999644337006636
-4,4	0.01173764938741580915572505702913
-5,5	0.00211976456798849884644315007219
-6,6	0.00026170845228301249011385925086
-7,7	0.00002208877826469659955769726449
-8,8	$1.2745253026359480126112714680367 \times 10^{-6}$
-9,9	$5.0275261810959383411581297192576 \times 10^{-8}$
-10,10	$1.3556297819769484757032262002820 \times 10^{-9}$
-11,11	$2.5012031341031852003279373539252 \times 10^{-11}$
-12,12	$3.1243604817078012360750317883072 \times 10^{-13}$
-13,13	$2.9655118189640940365948400709026 \times 10^{-15}$
-15,15	$5.5758174181938354491800200913102 \times 10^{-19}$

TABLE VII. D1Q20 Lattice with  $c_s = 1.8357424381402594$ 

$\mathbf{v}_i$	$w_i$
0	0.21731931022112109059537537887018
-1,1	0.18735357499686018912399983787195
-2,2	0.12004746243830897823022161375249
-3,3	0.05717041140835294313179190148076
-4,4	0.02023564183037203154174508370450
-5,5	0.00532341082536521716813053993040
-6,6	0.00104085519989277817787032717819
-7,7	0.00015125787069729717011289372472
-8,8	0.00001633702528266419558030012576
-9,9	$1.3114608069909806258412013955825 \times 10^{-6}$
-10,10	$7.8246508661616857867473666191193 \times 10^{-8}$
-11,11	$3.4697808952346470123102609636720 \times 10^{-9}$
-12,12	$1.1435779630395075964965610648417 \times 10^{-10}$
-13,13	$2.8013182217362421082623834683491 \times 10^{-12}$
-14,14	$5.0995884226301388644438757982605 \times 10^{-14}$
-15,15	$6.9079520892785667788901676695952 \times 10^{-16}$
-16,16	$6.8680470174442627832690379600090 \times 10^{-18}$
-17,17	$5.7551467186859264824045886746476 \times 10^{-20}$
-19,19	$8.3761764243303081227469285304101 \times 10^{-24}$

TABLE VIII. D2Q4 Lattice with  $c_s = 0.60625445810016454$ 

$\mathbf{v}_i$	$w_i$
(0,0)	$w_0^2$
(0,±1),(±1,0)	$w_0 w_1$
(±1,±1)	$w_1 w_1$
(0,±3),(±3,0)	$w_0 w_3$
(±3,±1),(±1,±3)	$w_1 w_3$
(±3,±3)	$w_3^2$

## Appendix B: Algorithmic Details

The main algorithmic steps of the Lattice Wigner method are similar to those of the Lattice Boltzmann method. For reference, consider the lattice shown in Fig. 9. At each node (black circle) there are distribution functions  $\bar{W}_i$ , equilibrium distribution function  $\bar{W}_i^{eq}$  and source term distributions  $S_i$  where  $i = 1, 2, \dots, N_q$ .

Once the initial configuration of the  $\bar{W}_i$ ,  $\bar{W}_i^{eq}$  and  $S_i$  has been set, the scheme proceeds as follows:

1. (Collision step) From Eq. (14) calculate for every node and every  $i = 1, 2, \dots, N_q$  the so called collision term given by  $\bar{W}_i^*(\mathbf{x}, t) = \bar{W}_i(\mathbf{x}, t) + \delta t \Omega_i + \delta t S_i + \frac{\delta t}{2} (S_i(\mathbf{x}, t) - S_i(\mathbf{x} - \mathbf{v}_i \delta t, t - \delta t))$ .
2. (Streaming step) Observe that Eq. (14) can now be written as  $\bar{W}_i(\mathbf{x} + \mathbf{v}_i \delta t, t + \delta t) = \bar{W}_i^*(\mathbf{x}, t)$ . This relation can then be used to update every node for the time step  $t + \delta t$ .
3. (Macroscopic fields) With the newly updated distribution functions  $\bar{W}_i(\mathbf{x}, t + \delta t)$  the macroscopic fields can be calculated according to Eq. (12) and used to update the equilibrium distribution function and source term.

The steps 1,2,3 are iterated until convergence is reached. If the boundary conditions are expressed in terms of distributions, then it is adequate to impose them at the streaming step. If they are expressed in terms of

the macroscopic fields then the boundary conditions can be imposed during step 3. For further details see Eq. [55]

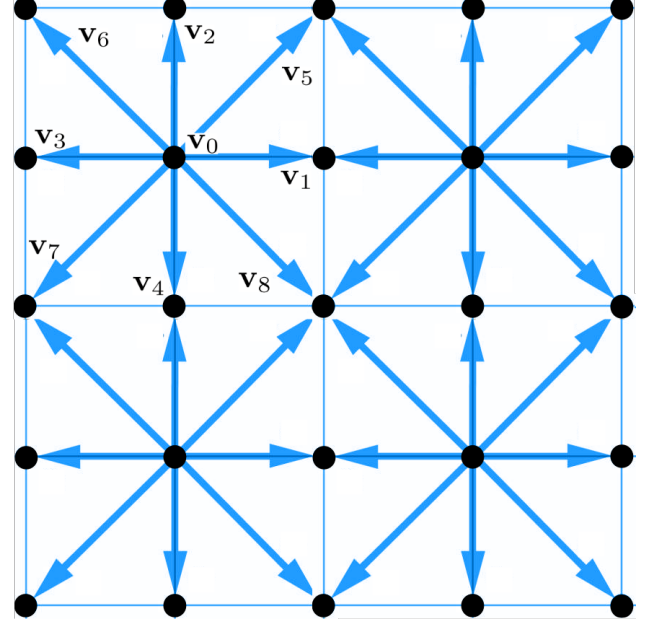


FIG. 9. (Color online) Scheme of a Lattice Wigner set up. The black circles denote the nodes where the multiple distributions are defined and the arrows show the velocity vectors.